ORIGINAL ARTICLE

Local surface smoothness on TC4 alloy during microbubbles flow electrolytic plasma polishing: prototype rig, phenomena, and mechanism

Juan Wang[1,2] · Huanwu Sun[1,3] · Dongliang Yang[1] · Gangqiang Ji[1] · Haidong Duan[1] · Yuxia Xiang[1]

Abstract

This paper introduces a microbubbles flow electrolytic plasma polishing (MF-EPP), which is based on electrolytic plasma polishing (EPP), but allows for local control polishing. MF-EPP energy consumption is lower, only 70–90 W power supply can complete the processing. Using Ti-6Al-4 V alloy sample as the polishing object, design and construct the original prototype to conduct theoretical and experimental research on the polishing process. The results show that the polishing solution has a stable polishing performance at a voltage of 210–430 V, functioning as a flexible polishing head, forming a circular polishing area of 14 mm in diameter on the workpiece surface, and reducing the surface roughness of polishing area from Ra 0.546 to 0.081 μm within 180 s. The processing phenomena, voltage and current characteristics, and surface morphology of the specimen are analyzed. Importantly, macroscopic and microscopic "pin-plate" models are proposed to elucidate the formation mechanism of MF (microbubbles flow) and the polishing mechanism of MF-EPP.

1 Introduction

Electrochemical polishing is an important surface treatment technique for metal materials, capable of reducing surface roughness and enhancing brightness [1–4]. Thus, the electrochemical polishing of TC4 alloys is a common post processing due to their widespread applications. However, traditional electrochemical polishing methods for titanium alloys often involve high concentrations of volatile, strong irritants and toxic chemicals, such as glacial acetic acid and hydrofluoric acid [5]. In 1979, the electrolytic plasma polishing (EPP) procedure was developed as a response to the hazardous nature of traditional methods. Unlike chemical and electrochemical polishing techniques that involve highly concentrated acid and caustic alkali solutions, EPP utilizes a low-concentration salt solution electrolyte, which results in the absence of harmful gases [6–12]. Furthermore, EPP offers numerous advantages over mechanical polishing, including excellent parts shape adaptability, no surface damage, no mechanical stress, and no thermal impact [6]. As a result, EPP has garnered increasing attention in recent years.

EPP actually refers to the classical Bath-EPP method, which involves immersing the part to be polished in a bath containing the polishing solution and connecting it as an anode. During the Bath-EPP process, both plasma and electrochemical reactions take place, resulting in a high material removal rate [7]. Hence, Bath-EPP has been successfully utilized for polishing various metal parts such as stainless steel, chromium and titanium alloys, aluminum, nickel-based superalloy, and zirconium-based bulk metallic glass [8–13]. Bath-EPP also has been successfully applied in additive manufacturing [14]. While Bath-EPP is effective at polishing the entire surface of a workpiece immersed in the electrolyte, it has limitations. One such limitation is the inability to achieve locally controlled polishing. Some studies have shown that Bath-EPP can be used to finish not only outer surfaces but also bore edges

✉ Huanwu Sun
  sunhuanwu@163.com

1   College of Mechanical and Vehicle Engineering, Taiyuan University of Technology, Taiyuan 030024, PR China

2   Department of Mechanical and Electrical Engineering, Shanxi Railway Vocational and Technical College, Taiyuan 030013, PR China

3   National Demonstration Center for Experimental Coal Resource and Mining Equipment Education, Taiyuan University of Technology, Taiyuan 030024, PR China

and internal bore walls down to a depth that corresponds to the bore radius in micro bones. Another limitation is that it cannot be used for polishing large-sized workpieces, as the maximum part size is limited by the capability of the process energy source [15]. This occurs because the process current is directly related to the surface area of the part submerged in the electrolyte. Furthermore, the polished workpiece exhibits poor surface consistency, as observed in submerged samples where the deeper regions experience a higher polishing rate compared to the upper regions closer to the electrolyte surface.

To overcome the above-mentioned limitations of Bath-EPP, a new method called jet (or spray) electrolytic plasma polishing (Jet-EPP or SEPP) has been developed in recent years [16–20]. The method entails using a cathodically polarized nozzle to direct a closed electrolytic jet toward the anodically polarized workpiece, eliminating the necessity of immersing the workpiece in the electrolytic bath. As a result, the size of the part being polished is no longer limited by the size of the polishing bath. Moreover, Jet-EPP allows for local polishing as the electrolyte jet hits the workpiece surface orthogonally, polishing only the hit area and keeping the rest of the surface in its original state. However, initiating the Jet-EPP process may not always be reliable with the available process energy sources, as they might not provide the required electric power with a sufficiently high current peak to start the process. This is an important consideration, as the process energy source plays a critical role in maintaining the sustainability of the polishing process, as noted by Parfenov et al. [19]. Electrolyte jet resistance increases linearly with the increasing working gap but decreases with quadratic dependency from the increasing nozzle diameter, which makes it difficult to manufacture suitable process energy source, as explained by Quitzke et al. To implement the Jet-EPP technique, a specialized process energy source capable of delivering sufficient electric current peaks up to 50 A was developed by Quitzke et al. [20]. The process is characterized by an electrolyte flow rate of 500 mL/min, a nozzle diameter of 5 mm, and a working gap of 6 mm.

Moreover, the design of the nozzle head shape plays a crucial role in the success of Jet-EPP. The nozzle head serves as the electrical contact between the feed line of the cathode and the electrolyte and determines the shape of the electrolyte jet shape. If the surface of the nozzle head is too rough or the design is suboptimal, it can result in a turbulent flow. The formation of sparks, arcs, and instabilities of the plasma is the consequence of Jet-EPP. Hence, recent research focused on nozzle head shape and electric resistance to mitigate these effects. However, creating plasma in a free electrolyte jet with a high flow velocity presents a challenge due to difficulties in accumulating charges [21]. Therefore, the development of new technologies of local surface smoothness is of utmost importance.

This paper presents a new EPP polishing technology, called microbubbles flow electrolyte plasma polishing (MF-EPP), to achieve local surface polishing of metal parts. In MF-EPP, a specialized process energy source and the nozzle are not obligatory, and the electrolyte flow rate is lower compared with Jet-EPP, almost drop by drop to the surface of the workpiece. The TC4 alloy serves as the polishing workpiece, on which MF-EPP created a circular polished area with a 14-mm diameter on its surface within 180 s. This resulted in a significant change in surface roughness and brightness in the local area. Through investigation of processing phenomena, voltage and current characteristics, and surface morphology of the specimen, two "pin-plate" models are proposed to elucidate the formation mechanism of microbubbles flow (MF) and the polishing mechanism of MF-EPP.

2 Experimental apparatus and method

2.1 Preparation of samples

TC4 alloy plates used in this study had a thickness of 3 mm with a chemical composition of Ti as the base, 6.6% Al, 4.9% V, 0.02% Zr, 0.033% Si, 0.18% Fe, 0.007% C, and 0.17% O. The samples were cut into smaller pieces with dimensions of 20 mm × 15 mm × 3 mm using the wire-electrode cutting method. Before experimentation, all samples were ground using a metallographic polishing machine (Weiyi MP-2) and silicon carbide abrasive papers with 120# grit to remove surface oxide and achieve a relatively uniform surface.

2.2 Design and setup of the prototype rig for MF-EPP

The setup consists of a control system, data acquisition system, kinematic system, electrical system, and electrolyte system. The control system is divided into three parts, namely voltage controller, electrolyte temperature controller, and working distance controller. The data acquisition system is responsible for collecting voltage and current signals, images of the polishing process, and the temperature in the processing area. Further, the kinematic system is mainly composed of a robot arm (Dobot Magician DT-MG-4R005-02E) to clamp the cathode that moves horizontally and vertically. The horizontal movement creates relative motion with the anode sample, facilitating selective local polishing of the surface of the anode sample. Meanwhile, the vertical movement adjusts the inter-electrode gap, which is controlled by the working distance controller. The working distance controller is built into the robot arm and controls the vertical distance by calibrating the start and end coordinates of cathode clamped the arm. The electrical system

is managed by the voltage controller which built into power supply and consists of wires, an electric clamp, and DC-regulated power supply (ITECH IT6018D), which serves as the process energy source. The power supply offers energy for the equipment with a voltage adjustment range of 0−1500 V. The maximum output electric current and power allowed by the power supply are 30 A and 18 kW.

The electrolyte system includes constant current injection pump (CFSP-I/CU-I) for transferring electrolytes from the tank to the drain, an electrolyte storage tank, a flow controller build into pump, and an electrolyte drain. The electrolyte storage tank is equipped with a heater (LiYuan electric heating rod U3KW2) and a temperature sensor. When the temperature of the electrolyte is less than 85 °C, the heater is activated. When the temperature exceeds 90 °C, the heater turns off, and the temperature control range is regulated by the electrolyte temperature controller. Figure 1 depicts the equipment and shape of the proposed MF-EPP prototype setup, along with its main components and their interconnections.

The pretreated TC4 alloy sample was secured on the working table and employed as the anode. Below the table, there was an electrolyte temperature control tank with an integrated temperature sensor and an automatic start-stop heater. This setup was used to maintain a constant temperature of the electrolyte. The cathode is made of a titanium wire with a diameter of 2 mm, with the electrolyte conduit bound to it, allowing the electrolyte to drip onto the surface of the sample along the cathode wire. A mechanical arm is employed to move the cathode and electrolyte conduit along a path for selective polishing while precisely controlling the working distance between the cathode and anode.

The process energy source used in the MF-EPP process is Edex IT6015D high-power DC-regulated power, which is similar to the one used in Bath-EPP and does not need a custom high-power supply.

Under the effect of high DC voltage, the electrolyte between the anode and cathode forms MF, which polishes the local area of the sample it covers. After the MF-EPP process, the sample was rinsed with anhydrous ethanol and deionized water multiple times to remove the residual electrolytes on the surface.

Table 1 shows the process parameters used in MF-EPP, with the DC-regulated power supply as the energy source. The polishing effectiveness and electrolyte shape are directly influenced by the voltage. To ensure experimental repeatability, three samples were processed under each condition. It is important to mention that the electrolyte type should be compatible with the metal being polished [15, 22]. When choosing electrolytes for MF-EPP processing, it is recommended to refer to the EPP electrolytes used for polishing the specific metal [15].

2.3 Test and characterization

A high-definition camera was utilized to record the polishing procedure. The Fluke Ti401 PRO thermal imaging device was used to record the temperature distribution throughout the process. The test temperature was ambient temperature, which was about 15.5 °C. In order to minimize the influence of the system error, sensitivity, and temperature measurement accuracy of the thermal imaging device with the change in ambient temperature, all polish processing experiments in this paper were carried out on the same
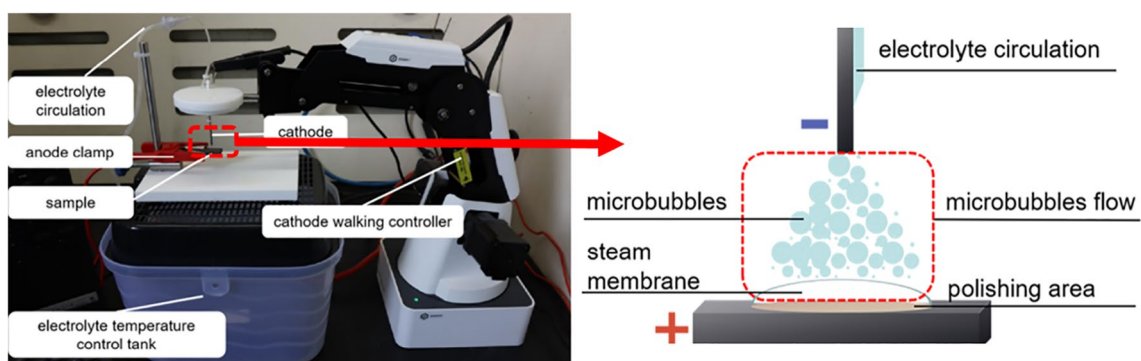

Fig. 1 MF-EPP prototype and shape of MF

Table 1 Process parameters of MF-EPP

Temperature of electrolyte	Base solution	Content of electrolyte	Inter-electrode gap	Time	Cathode diameter	Electrolyte flow rate
85–90 °C	H_2O	3%	4 mm	180 s	2 mm	0.3–0.4 mL/s

day and same place. The colors exhibited in the thermal image denote distinct temperature ranges of the object under assessment. The temperature was calculated as the mean temperature within a specific region.

The surface characteristics of the samples were examined using the Leica DVM6 microscope, which provides an extensive depth of field. The variation in surface roughness of the samples was determined using the MarSurf M400 surface roughness instrument made in Germany. During the roughness measurement, five horizontal and five longitudinal positions of the polished area were selected for testing each sample. The Ra (arithmetic mean deviation of contour), Rq (root mean square deviation of contour), and Rz (maximum height of contour) were recorded. Subsequently, the average values were calculated to represent the surface roughness characterization. For ease of discussion in this study, the average current of the MF, which denotes the instantaneous circuit current of the system, was used. The weight change of the samples before and after MF-EPP was measured using digital electronic scales (FA2004). All the material removal rate tests were repeated three times (keeping all other experimental conditions constant except voltage) to ensure the reliability of the data.

3 Experimental results and analysis

3.1 Phenomena of the experimental process

The voltage is the key factor in determining whether MF can be formed and whether polishing can take place. Therefore, by setting different values of voltage, the phenomenon of the experimental process is observed. Figure 2 presents the electrolyte shape and the sample surface state at different voltages. When the voltage was set at 0, the electrolyte appeared as a transparent liquid, as depicted in Fig. 2(a). On the other hand, the cathode, anode, and electrolyte showed evident microbubbles of a micron or smaller size at a voltage of 20 V (Fig. 2(b)). This was due to the electrolytic reaction, in which hydrogen and oxygen were generated at the cathode and anode and entered the electrolyte [7]. At the same time, the anode sample began to oxidize under the effect of the electrolytic reaction, leading to the formation of colored oxide on its surface. As the voltage continued to increase, the electrolytic reaction intensified, leading to a significant increase in the number of microbubbles on the anode surface and in the electrolyte. The oxidation phenomenon on the anode surface became more pronounced, as shown in Fig. 2(c) and (d).

Further, as the voltage was increased to 300 V, the size of individual microbubbles in the electrolyte increased, resulting in an overall increase in the volume of the electrolyte in the working area. Notably, the electrolyte formed a cone shape on the surface of the anode sample, as depicted in Fig. 2(e).

Nevertheless, when the voltage surpassed a critical value, the diameter of a single microbubble in the working zone of the electrolyte reduced significantly compared to Fig. 2(e). Moreover, the electrolyte no longer remained dispersed, but transformed into a cluster of gas–liquid mixed states with well-defined outer edges, suspended on the steam membrane, as illustrated in Fig. 2(f), which is MF state.

At this stage, an acoustic bang occurred. As the MF left the working area, it returned to its fluid state. With a further increment in voltage, an orange-yellow glow was observed on the surface of the anode sample (Fig. 2(g)). This corresponds to the results of Yerokhin et al. [23], who detected this effect and explained it with contact glow discharge electrolysis. As the voltage continued to rise, the discharge phenomenon became more severe, as shown in Fig. 2(h).

Thermal imaging of the MF-EPP process was analyzed to obtain the location of the heat production and the mode of heat transfer. The thermal image displayed in Fig. 3 was captured at a voltage of 100 V and 350 V. At the voltage of 350 V, the steam membrane of the MF was stable, and the surface quality of the processed sample was superior to that of other voltages. It was noticed that the temperature of the steam membrane was 98.4 °C, which was higher compared to the microbubbles (ranging from 89.4 to 98.4 °C) above it. In addition, the temperature of the MF in the working area was greater than that of the electrolyte in the system (85−89 °C). These findings indicated that the heat was generated due to the contact position between the steam membrane and the sample, followed by the heat transfer. The temperature at the interface between the anode sample and the MF was observed to be approximately the boiling point of water. Notably, the highest temperature position was consistent with the position of the steam membrane, as shown in Fig. 2(f)–(h).

It was evident that the formation of the MF is an essential requirement for MF-EPP. MF is a cluster of gas–liquid mixed states with well-defined outer edges, include and suspend on the steam membrane.

3.2 Current and resistance characteristics with voltage

In order to achieve the locally polishing of the sample, the electrode arrangement of MF-EPP followed a "pin-plate" structure, with the needle as the cathode and the plate as the anode. The electrolyte flowed down from the cathode, cooling the cathode and forming a steam membrane on the surface of the sample. By gradually increasing the voltage applied to the titanium wire and plate sample, the current and resistance data were recorded. Figure 4 shows the

Fig. 2 Photograph of electrolyte shapes at different voltages
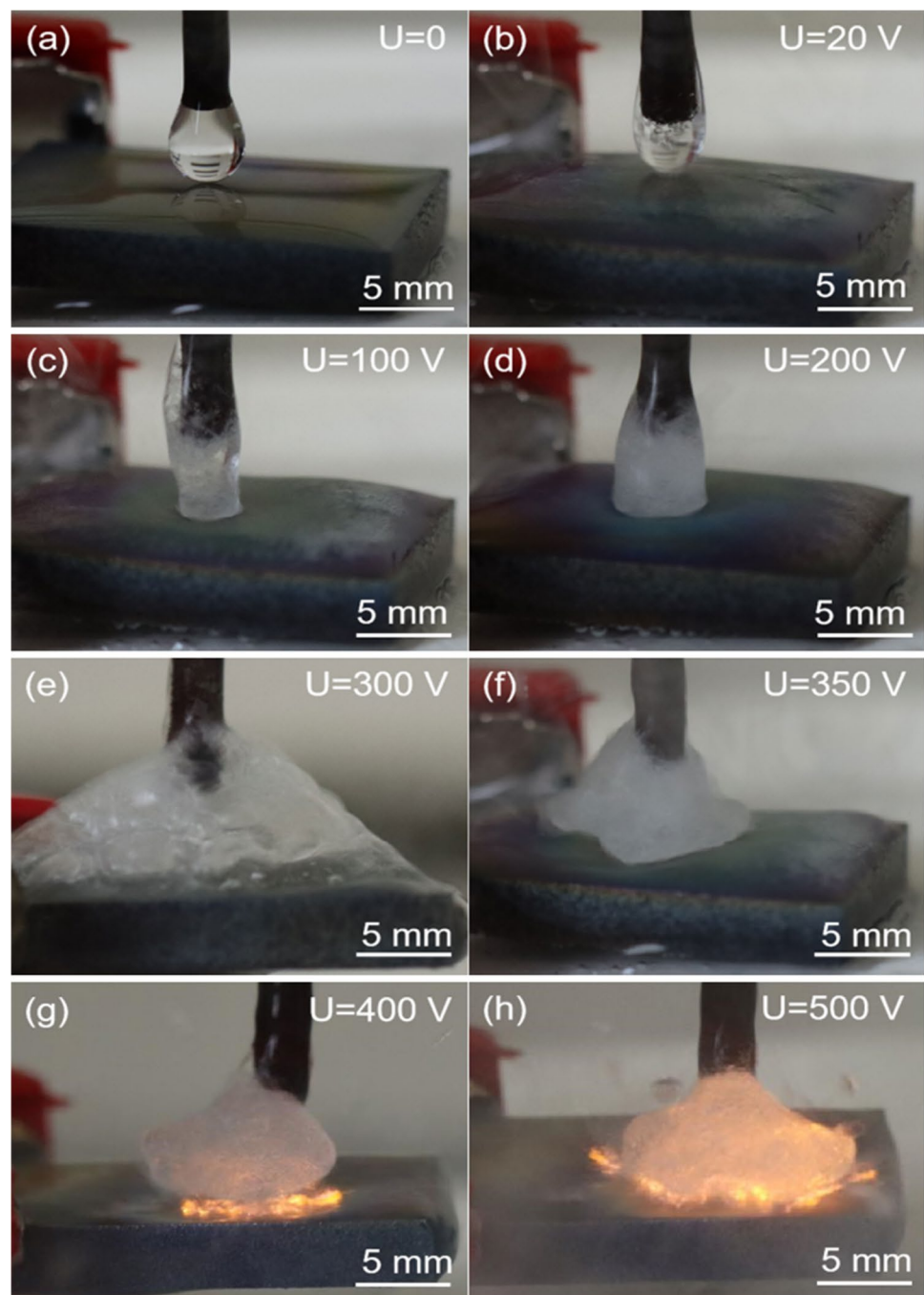
resulting characteristic curves of current and resistance as a function of voltage.

By comparing the electrolyte shapes at the corresponding voltage in Fig. 2, the formation mechanism of MF can be inferred from the voltage and current curve, which was divided into four stages. Figure 4 displays that during Stage I, microbubble formation stage, the voltage ranged from 0 to 150 V, and the current was nearly proportional to the applied voltage. At this stage (Fig. 2(b) and (c)), microbubbles of micrometer size were intermittently generated from

the sample surface and cathode into the polishing liquid. The resistance remained constant, mainly due to the resistance of the electrolyte and wire, making it a classic electrolysis mode. Based on the principles of electrochemistry and heat transfer, microbubbles are classified into two categories. The first type is formed when gas trapped in tiny surface holes is heated to create microbubbles. These microbubbles are primarily composed of water vapor and occur on rough material surfaces. The second type is formed during electrolytic reactions on the anode and the cathode. Oxygen

Fig. 3 Distribution of temperature field, (a) at 100 V and (b) at 350 V
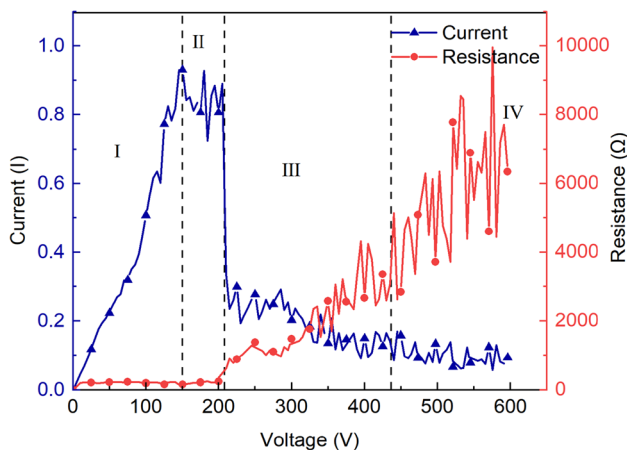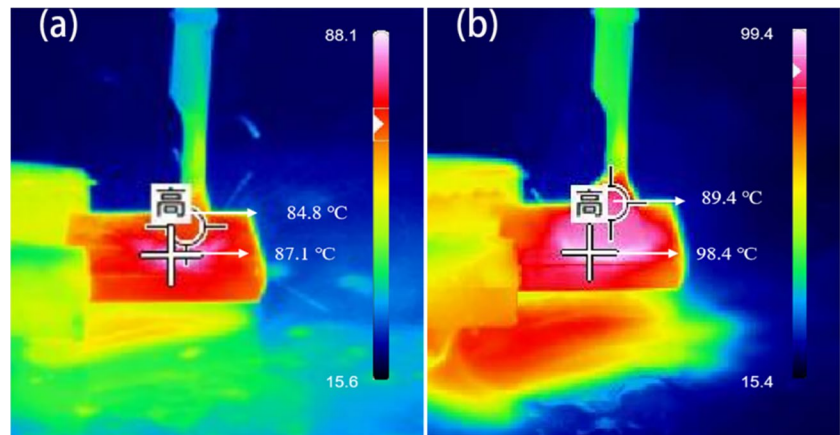

Fig. 4 Curve of current and resistance as a function of voltage

microbubbles are formed on the surface of the anode, while hydrogen microbubbles are formed on the cathode. These bubbles mix with the electrolyte, creating a gas–liquid two-phase flow.

In Stage II, the microbubbles fusion stage, the voltage ranged from 150 to 210 V. At this stage, with increasing voltage, the resistance and current remained relatively constant. The rate of bubble formation also increased. However, the rate of bubble escape was lower than the rate of formation, resulting in the formation of a string of bubbles that fused together at certain locations on the sample surface. On a macro level, the volume of the electrolytic in droplet shape also increased too, as depicted in Fig. 2(d).

During Stage III, the MF stage, which included both the formation of MF and stabilization of MF, the voltage range was between 210 and 430 V. As observed in Fig. 4, the current was not increased with increasing voltage but instead significantly decreased. This was attributed to the formation of many small vapor films on the sample surface after the fusion of microbubbles. The formation of these small vapor films increased the resistance, while their instability caused

the resistance to fluctuate considerably, resulting in a large fluctuation in the current. At this stage, the small vapor film was not yet capable of completely isolating the sample from the electrolyte, and the processing phenomenon observed is shown in Fig. 2(e). This stage is referred to as the MF formation stage. When the voltage was greater than 300 V but less than 430 V, the MF entered the stability stage, during which a relatively stable steam membrane was formed. As the voltage continued to increase, the heat generated by the system surpassed the critical heat flux emitted by the sample surface, causing the part of the electrolyte and sample in contact to boil quickly and form a complete steam membrane that almost completely isolated the electrolyte from the sample. Consequently, the resistance between the cathode electrolyte and the anode sample increased significantly, leading to a decrease in current as the voltage increased. Figure 2(f) and (g) present the corresponding phenomenon.

During the last Stage IV, which is the MF instability stage, the resistance became unstable as the voltage exceeded 430 V, as shown in Fig. 4. This was due to the occurrence of a strong discharge phenomenon on the sample surface, which disrupted the stability of the underlying steam membrane of the MF, and caused the resistance to become unstable. This is illustrated in Fig. 2(h).

3.3 Current characteristics with time

Based on the current and resistance analysis presented above, as well as the processing phenomenon shown in Fig. 2, five distinct voltages (U = 20 V, 100 V, 200 V, 300 V, 350 V, 400 V) were selected. To establish a consistent contact between the steam membrane and the sample surfaces, specific samples were selected for the application of the previously mentioned voltages. Each voltage was applied for a duration of 180 s to both the titanium wire pin and the plate sample. The resulting alterations in current under constant voltage conditions were documented. Figure 5 illustrates the current patterns over time at various voltage levels. It
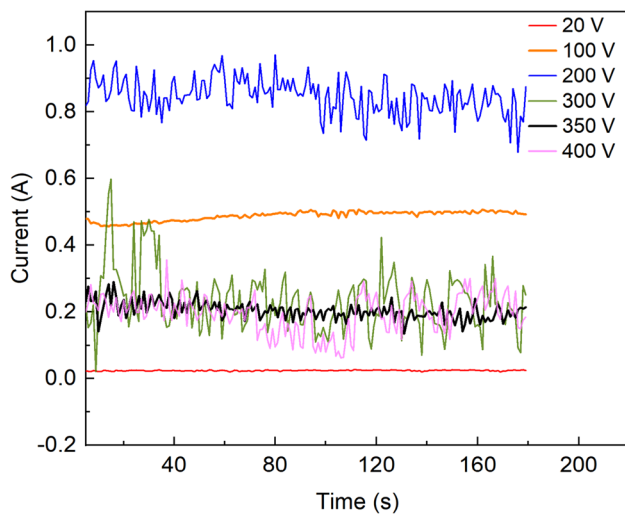
Fig. 5 Curve of current with time at different voltages

is worth highlighting that the processing encountered instability and manifested a pronounced discharge phenomenon when the voltage surpassed 430 V. Consequently, no current curve was attainable beyond this voltage threshold.

At a voltage of 20 V, the current ranged from 0.0186 to 0.0259 A. When the voltage was increased to 100 V, the current was 0.4574−0.5071 A, which was higher than that at 20 V. This indicated Stage I. It can be seen from Fig. 5 that the current fluctuations at these two voltages were minimal. At U = 200 V, which was Stage II, the current observed was 0.6109−0.9534 A, demonstrating a significant increase and large fluctuations. These drastic changes were attributed to the fusion and rupture of microbubbles, which caused the variation in the conductivity of the electrolyte. Although the vapor film was not yet formed, the current remained high. Moreover, at U = 300 V, the current ranged from 0.0212 to 0.5982 A, while at 400 V, the current ranged from 0.0767 to 0.2981 A. This was Stage III. Noticeably, the current value was less than that at 200 V, but with large fluctuations. This was due to the intermittent separation of the sample from the electrolyte by the steam membrane in MF, leading to an intermittent change in resistance. It is worth noting that the smallest current fluctuation of 0.1672−0.2904 A was observed at a voltage of 350 V. This was attributed to the formation of a relatively stable steam membrane under this condition, resulting in a slight resistance fluctuation and, subsequently, a small current fluctuation. Therefore, the surface quality of the machined parts was the best under this condition in a given processing time.

Based on the aforementioned observations, it can be deduced that the steam membrane exhibited irregular cycles of formation and rupture throughout the MF-EPP procedure. The creation and breaking of bubbles and the steam membrane had an impact on the transfer of charge. Concurrently, the steadiness of the steam membrane influenced fluctuations in current. As a result, alterations and oscillations in current over time partly mirrored the stability of the steam membrane and the efficacy of the machining process.

3.4 Surface morphology

In order to study the polishing effect at different stages of the process, the surface morphology of the material surface in the polished area was analyzed. As observed in Fig. 6(a), the scratches observed in the untreated image can be attributed to the mechanical grinding process. During Stage I, which followed the classic electrolysis mode as discussed in Section 3.2, the surface image of the sample (as shown in Fig. 6(b)) clearly indicated the presence of colored electrolytic products on the sample surface. The trenches and plowing marks from the mechanical slip were still present and not reduced. The surface image of the sample in Stage II is depicted in Fig. 6(c). In this stage, although the trenches and plows on the sample surface were somewhat reduced, colored electrolytic products were still visible. Furthermore, at the MF stage (Stage III), the surface image of the samples after MF-EPP processing is shown in Fig. 6(d). The trenches and plows from mechanical slip on the surface of the samples were basically smoothed out.

Surprisingly, at a voltage of 500 V, the MF entered the instability stage, resulting in intense micro-arc discharge and occasional spark generation that destroyed the sample surface. Figure 6(e) clearly shows traces of melted and resolidified surface material at the position of electrical spark discharge on the specimen surface. Under this condition, the surface was pitted by the spark discharge, leading to uneven surface quality.

3.5 Surface roughness

In order to investigate the role of electrochemical and plasma action on local polishing, the roughness values of the surface of the sample processed at different stages were studied. Figure 7 depicts the variation of the local surface roughness Ra of the sample at different voltages. It was observed that the Ra of the sample was higher than that of the untreated sample when the voltage was at Stages I and II.

This could be attributed to the absence of MF formation under those conditions, where electrochemical reactions predominantly occurred on the surface of the sample. As a result, the electrochemical oxidation rate was higher than the electrochemical dissolution rate, resulting in the attachment of electrochemical products to the surface of the samples.

As the voltage at Stage III, MF was formed, leading to a considerable decrease in Ra in the area covered by MF. This confirmed that the area covered by the MF had undergone polishing. This was due to the reaction between the

Fig. 6 Optical microscopic image and 3D topography of the samples, (a) untreated, (b) Stage I, (c) Stage II, (d) Stage III, and (e) Stage IV
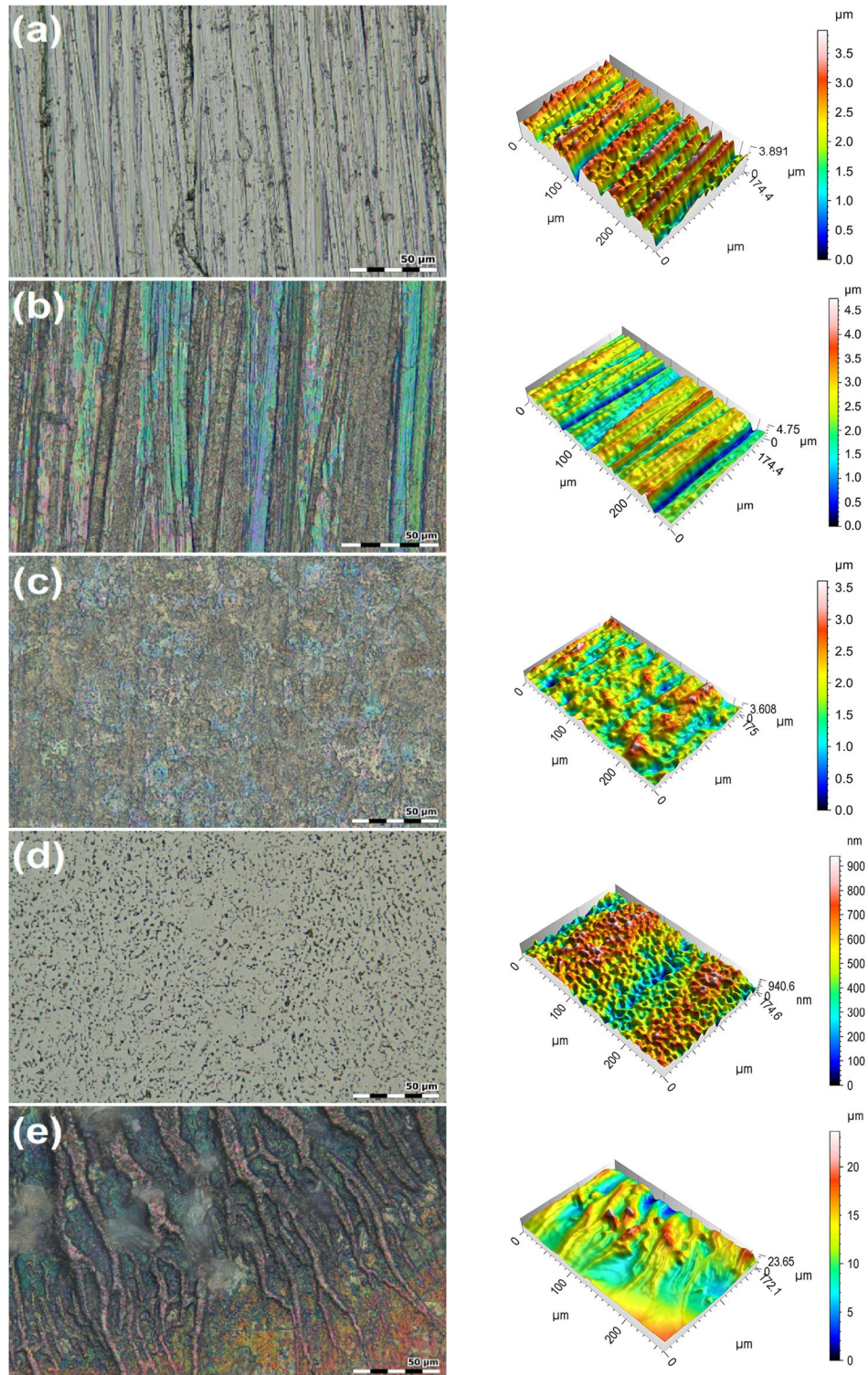
MF and the surface covered by it, resulting in the removal of electrochemical products by the MF. However, when the voltage was set under Stage IV, the discharge phenomenon was severe, leading to uneven surface quality, and making it pointless to calculate the surface roughness of the sample under this condition.

Based on the above observations, it was concluded that electrochemical reactions alone were insufficient to achieve effective polishing of the sample, and thus MF played an important role in the process.

Figure 8 demonstrates the reduction of the local surface roughness during MF-EPP. The specimen surface exhibited
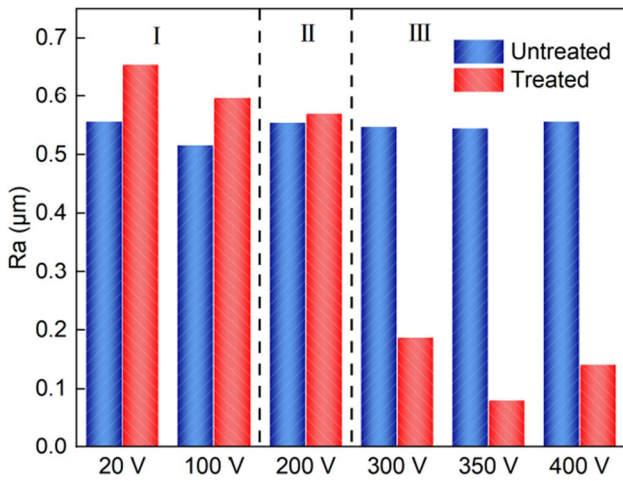
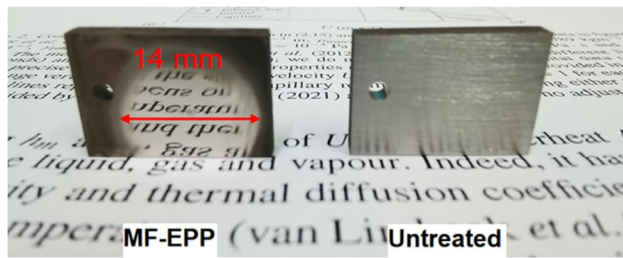**Fig. 7** Roughness of the sample before and after the treatment

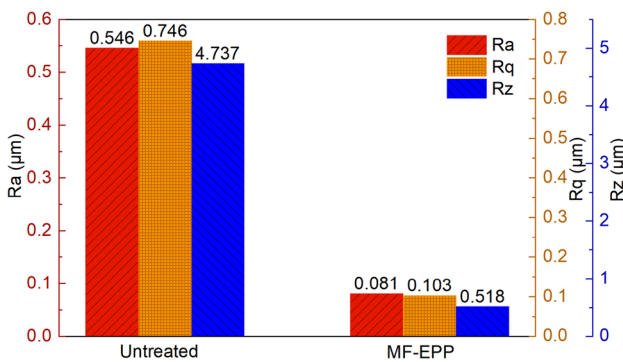**Fig. 8** MF-EPP processed TC4 sample

Fig. 9 Surface roughness parameters of the sample

noticeable mechanical grinding marks before the treatment. However, after the MF-EPP processing at a voltage of 350 V, the mechanical grinding marks in the central region of the sample disappeared completely. Additionally, the reflection in the polished area became apparent, while the reflection in the surrounding region remained low.

Further, the local surface roughness parameters Ra, Rq, and Rz of the sample decreased significantly after the processing. Figure 9 presents the surface roughness
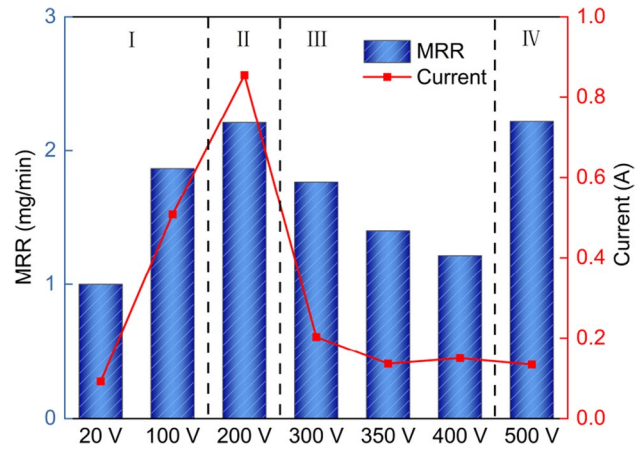

Fig. 10 MRR at different stages

parameters of the sample before and after processing at a voltage of 350 V, using the process parameters outlined in Table 1.

3.6 Material removal rate

In order to investigate the material removal rate (MRR) at different stages, weight change of the samples before and after MF-EPP at different stages was recorded. The MRR (mg/min) can be calculated by the following formula:

$$MRR = \frac{\Delta m}{t} \tag{1}$$

where Δm (mg) is the weight change of the samples before and after MF-EPP; t (min) is the processing time.

Figure 10 depicts the variation of the MRR at different stages. It has been shown that as the voltage increased, the MRR also increased until it reached Stage II, after which it decreased. The trend of MRR was very similar to the trend of current with voltage in Fig. 4. This was also consistent with Faraday's first law of electrolysis.

However, an anomaly phenomenon occurred in Stage IV, where the average current in the system was at a low level, the MRR increased significantly. This may be due to the following reasons. At Stage IV, the MF entered the instability stage, representing the average value of the current was small, and the amplitude indeed increased significantly, as shown in Fig. 4. At this stage, intense micro-arc discharge and occasional electrical spark generation destroyed the sample surface, as shown in Fig. 6(e). The surface of the sample exhibited melted and resolidified pits, indicating that Stage IV no longer reflected polishing performance but instead belonged to electrical discharge machining.

4 Discussion

Based on all the experimental results and analysis, two "pin-plate" models are proposed to elucidate the phenomena and characteristics of MF and the polishing mechanism of MF-EPP. The first model is a macro "pin-plate" model that utilizes a cathode titanium needle as the "pin" and the anode sample as the "plate." This negative "pin-plate" model is primarily employed to explain the phenomena and characteristics of MF. The second model is a micro "pin-plate" model, which considers the cathode regional steam membrane in MF as the "plate," and the microscopic mountains on the surface of the anode as the "pin." This model establishes numerous microscopic positive "pin-plate" models and clarifies how the local sample surface is smoothed and polished via MF-EPP.

4.1 Macroscopic "pin-plate" model

Based on the experimental results in Section 3, it was evident that the electrolyte exhibited significant polishing properties solely during the formation and stabilization stages of MF (Stage III). Therefore, it is imperative to examine the formation of MF. Figure 11 illustrates the formation process and structural features of MF. It can be seen from Fig. 2(f) and (g), MF consisted of an irregular pattern of the steam membranes near the sample surface and a cluster of gas–liquid mixtures above the steam membrane.

During Stage I, the Ohmic heating caused the water to vaporize, resulting in the formation of some microbubbles:

$$H_2O + heat \rightarrow H_2O_{gas} \uparrow \tag{2}$$

At the same time, oxygen was precipitated on the anode surface due to an electrolytic reaction, forming microbubbles:

$$4OH^- \rightarrow O_2 \uparrow + 2H_2O + 4e^- \tag{3}$$
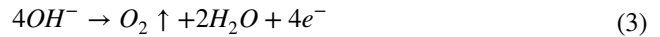
In addition, hydrogen was precipitated on the cathode surface because of an electrolytic reaction, forming microbubbles:

$$2H_2O + 2e^- \rightarrow 2OH^- + H_2 \uparrow \tag{4}$$

Those three types of microbubbles mentioned above were transferred into the electrolyte water. This was observed in Fig. 2(b) and (c), which showed obvious microbubbles generation at the cathode and anode. Based on "bubble" model in liquid-phase plasma discharge [24–26], when the "microbubble" was breaking down, heat would have been generated. After the microbubble breakdown, fresh electrolyte flowed to the sample surface to create a new "microbubble." This new microbubble then underwent the same breakdown process, and the cycle continued.

During Stage II, with the voltage increasing, the Ohmic heating and oxygen evolution reaction were increased. Due to those, numerous microbubbles were generated near the anode, microbubbles begin to fuse and merge [7, 23]. The Ohmic heating increased the temperature of the electrolyte and the specimen. As shown in Fig. 3(a), the electrolyte temperature near the sample was higher than it in the system.

One of the notable features of MF-EPP is the low flow rate of electrolyte, which almost trickles on the sample surface. Consequently, the added heat can easily bring the droplets to the boiling point. So at Stage III-1, namely the MF formation stage, nuclear boiling occurred (Fig. 2(e)). Further, once the electrolyte reached boiling point, its heat

Fig. 11 Macro "pin-plate" model
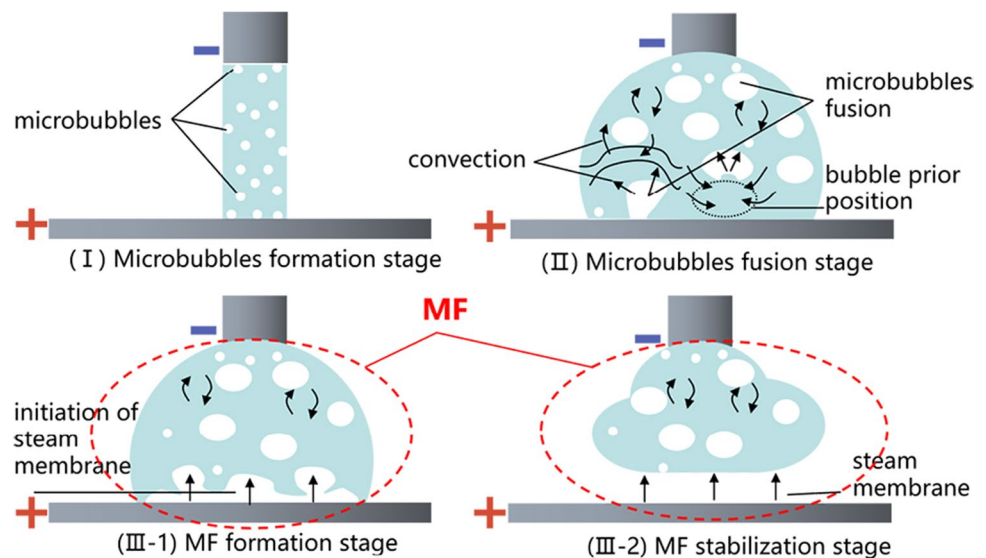
absorption capacity was reduced. Due to this, the heat generated at this stage was mainly absorbed by the sample surface. Because of the macro "pin-plate" model, the electric field was not evenly distributed, resulting in localized high temperatures in areas with strong electric fields. So the place where owning localized high temperatures formed a regional steam membrane over the sample surface, as illustrated in Fig. 2(f) and (g). This corresponded to Stage III-2, namely the MF stabilization stage.

The thickness, dimensions, and position of the steam membrane experienced influence from the electric field arrangement established by the macroscopic "pin-plate" model. This steam membrane functioned as an obstruction separating the specific surface of the sample and the electrolyte. When a sufficient amount of electrical charge accumulated on either side of the localized steam membrane, a strong electric field, a potential difference was created, and plasma discharge phenomenon occurred. Plasma discharge is often accompanied by high temperature and pressure instantaneously [7]. High temperature would rise the volume of steam membrane. High pressure would produce a shock wave to make the steam membrane broken down. Then, a new cycle was initiated by the influx of fresh electrolyte onto the sample surface.

Hence, the main heat sources for the formation of the regional steam membrane were Ohmic heat. Besides, the primary constituents of the regional steam membrane were water vapor and oxygen. The steam membrane intermittently made contact with the regional surface of the sample, as confirmed by the time-dependent curve of current in Fig. 5 and analyzed in Section 3.3.

4.2 Microscopic "pin-plate" model

The second model, the microscopic "pin-plate" model, was applied after the formation of the MF. In this model, the cathode steam membrane acted as the "plate," and the microscopic mountains on the surface of the anode sample acted as the "pin," forming many microscopic positive "pin-plate" models (Fig. 12). As explained in Section 4.1, the steam membrane produced intermittent contact with the regional surface of the sample.

When the steam membrane broke down, the electrolyte made contact with the sample and underwent an electrochemical reaction. Both electrochemical oxidation and dissolution reactions occurred simultaneously. The formation of electrolytic oxides involves the dissolution of metal ions into solution, as described by the following equation:
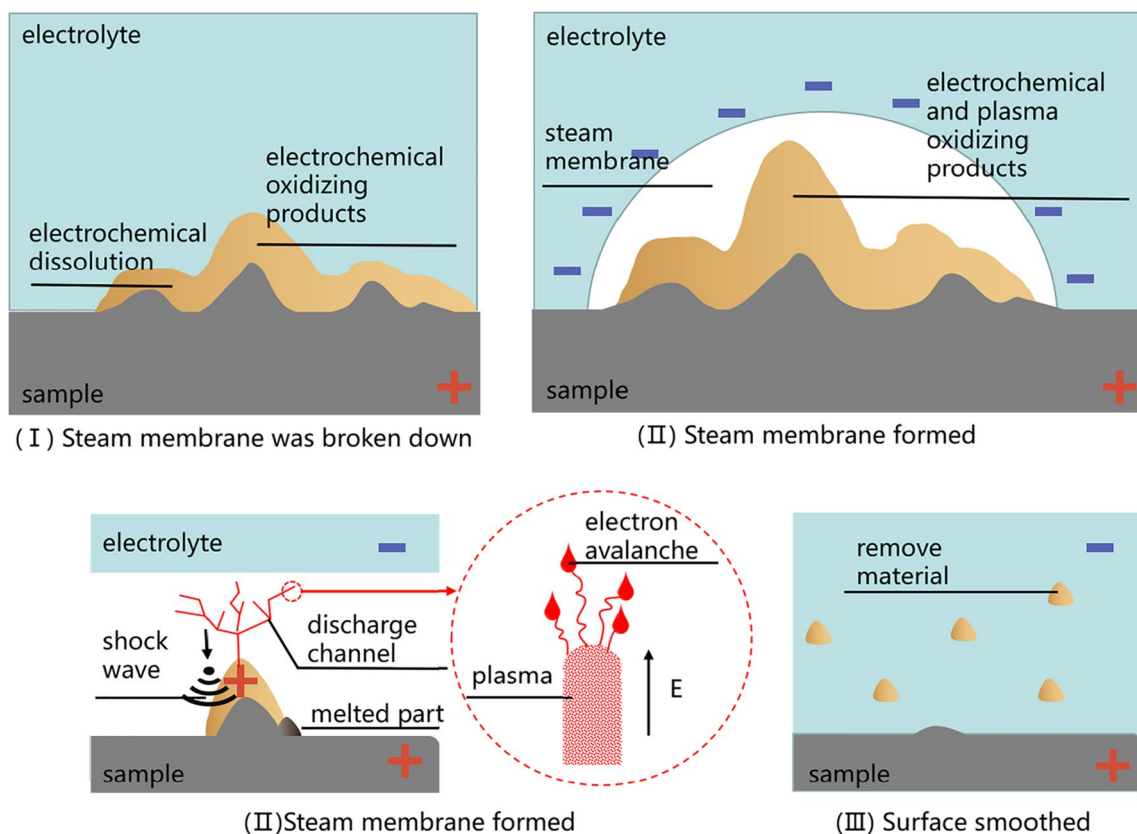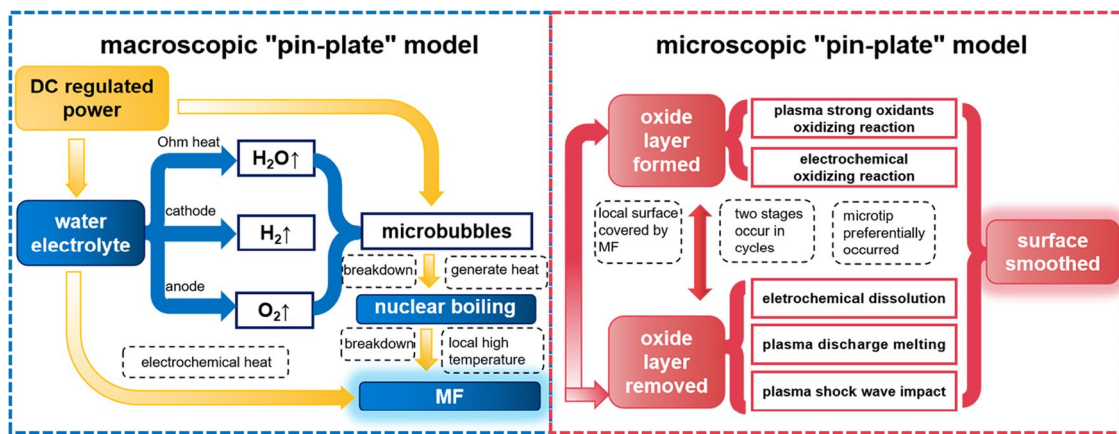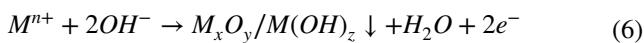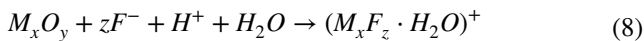

Fig. 12 Micro "pin-plate" model

Fig. 13 Flow diagram of local surface smoothness evolution by MF-EPP

$$M \rightarrow M^{n+} + ne^- \tag{5}$$

The electrolytic oxide layer was formed on the anode surface through the following reaction [15]:

$$M^{n+} + 2OH^- \rightarrow M_xO_y/M(OH)_z \downarrow + H_2O + 2e^- \tag{6}$$

$$xM^{n+} + yF^- \rightarrow M_xF_y \downarrow \tag{7}$$

The electrochemical dissolution reaction occurred as follows [27]:

$$M_xO_y + zF^- + H^+ + H_2O \rightarrow (M_xF_z \cdot H_2O)^+ \tag{8}$$

where M is the metal, and F is the anion of the electrolyte.

The rate of electrochemical oxidation exceeded the rate of electrochemical dissolution, with a higher rate of electrochemical oxidation at the peak than in the pit. Consequently, in the absence of the steam membrane, the surface roughness of the sample increased, as shown in Fig. 7.

When the steam membrane formed, it resulted in most of the voltage being applied to both sides of it. The accumulation of charges at both ends of the steam membrane during its formation resulted in local high voltage. Meanwhile, the steam membrane at the bottom of the MF provided conditions for the generation of plasma [23, 27–29]. Potent oxidizing agents within the plasma prompted the segment of the sample surface enveloped by the steam membrane to develop plasma oxides. The concentrated current density at the microtip made it uncomplicated to establish localized high voltage. Significantly, the phenomenon of gas discharge transpired solely when the current traversed through the steam membrane under elevated voltage. This allowed the current to progress from passed through the steam membrane impinged on the cusp in the form of an ion beam, resulting in plasma oxidation and physical impact on the

microtip [15]. So the microtips on the surface were preferentially removed [30].

To summarize, the previous discussion revealed the local surface smoothness evolution by MF-EPP. It consists of two processes: the oxide layer formed and oxide layer removed. The oxide layer on the sample surface was formed due to the electrochemical reaction and oxidation caused by strong oxidizing substance produced by plasma discharge. This oxide layer was removed by electrochemical dissolution and plasma impact in the region covered by the MF. Furthermore, since the probability of plasma discharge channel formation was higher in the mountains than in the pits, the amount of material removed in the mountains was consistently greater than that in the pits. This led to the microscopic leveling of the local surface covered by the MF. The flow diagram of the local surface smooth evolution is shown in Fig. 13.

5 Conclusion

This study investigated the MF-EPP technology as an innovative approach for localized polishing. It compared and analyzed the shape of the MF, the outcomes of polishing, and the fluctuations in current signals under varying voltages. The key findings of the research can be summarized as follows:

Through the examination of current signal fluctuations with linearly increasing voltage and the analysis of the electrolyte's shape at different voltages, the progression of the electrolyte's behavior was categorized into four stages: the microbubble formation stage, microbubble fusion stage, MF stage, and MF instability stage. The experimental outcomes indicated that the MF was generated and displayed stable polishing traits within a specific voltage range (210−430 V).

Consequently, the sample surface underwent selective polishing within areas where the MF was present.

By evaluating the shape of the MF, we introduced a definition and the structural characteristics of MF, which distinguish it from other gas–liquid two-phase flows. MF takes the form of a cone-shaped cloud-like gas–liquid two-phase flow. It comprises an irregular pattern of the steam membrane in proximity to the sample and a cluster of gas–liquid mixtures situated above the steam membrane. MF intermittently makes contact with the local surface of the sample, creating the necessary conditions and environment for electrochemical reactions and plasma generation.

Two models labeled as "pin-plate" models were put forth, grounded in the principles of liquid-phase plasma discharge and boiling heat transfer. The first model was a macroscopic "pin-plate" model, while the second one was a microscopic "pin-plate" model. These models elucidated the factors contributing to MF formation, the shape of MF, and the progression of local surface smoothness.

Data availability Not applicable.

Code availability Not applicable.

Declarations

Ethics approval Not applicable.

Consent to participate Not applicable.

Consent for publication Not applicable.

Conflict of interest The authors declare no competing interests.

References

1. Mu JR, Sun TT, Chu LAL, Oliveira JP, Wu Y, Wang HW, Wang HZ (2023) Application of electrochemical polishing in surface treatment of additively manufactured structures: a review. Prog Mater Sci 136:101109. https://doi.org/10.1016/j.pmatsci.2023.101109

2. Han W, Fang FZ (2019) Fundamental aspects and recent developments in electropolishing. Int J Mach Tools Manuf 139:1–23. https://doi.org/10.1016/j.ijmachtools.2019.01.001

3. Baldhoff T, Nock V, Marshall AT (2018) Review—Through-mask electrochemical micromachining. J Electrochem Soc 165:E841–E855. https://doi.org/10.1149/2.1341814jes

4. Zou YC, Wang SQ, Chen GL, Wang YM, Zhang KW, Zhang CR, Wei DQ, Ouyang JH, Jia DC, Zhou Y (2023) Optimization and mechanism of precise finishing of TC4 alloy by plasma electrolytic polishing. Surf Coat Technol 467:129696. https://doi.org/10.1016/j.surfcoat.2023.129696

5. Wang SF, Wang Y, Wen JC, Suo HL, Liu ZZ, Suo WH, Zhao CC (2021) Study on electrochemical polishing of TC4 alloy. Mater Res Express 8:106520. https://doi.org/10.1088/2053-1591/ac1f4c

6. Ji GQ, Sun HW, Duan HD, Yang DL, Sun JY (2021) Effect of electrolytic plasma polishing on microstructural evolution and tensile properties of 316L stainless steel. Surf Coat Technol 420:127330. https://doi.org/10.1016/j.surfcoat.2021.127330

7. Zhou CQ, Su YH, Qian N, Zhang Z, Xu JH (2022) Characteristics and function of vapour gaseous envelope fluctuation in plasma electrolytic polishing. Int J Adv Manuf Technol 119:7815–7825. https://doi.org/10.1007/s00170-021-08606-x

8. Ji GQ, Sun HW, Duan HD, Yang DL, Sun JY (2023) Enhancement of corrosion resistance for medical grade 316L stainless steel by electrolytic plasma polishing. J Mater Eng Perform 32:1498–1507. https://doi.org/10.1007/s11665-022-07206-4

9. Muratov KR, Gashev EA, Ablyaz TR (2022) Recommendations for electrolytic plasma polishing of chromium and titanium alloys. Russ Engin Res 42:829–831. https://doi.org/10.3103/S1068798X22080172

10. Schulze HP, Zeidler H, Kröning O, Böttger-Hiller F, Herzig M (2022) Process analysis of plasma-electrolytic polishing (PeP) of forming tools. Int J Mater Form 15:6. https://doi.org/10.1007/s12289-022-01659-7

11. Spica A, Roche J, Arurault L, Horville M, Rolet J (2021) Evolution of model roughness on quasi-pure aluminum during plasma electrolytic polishing. Surf Coat Technol 428:127839. https://doi.org/10.1016/j.surfcoat.2021.127839

12. Zhou C, Qian N, Su H, Zhang Z, Ding WF, Xu JH (2022) Effect of energy distribution on the machining efficiency and surface morphology of Inconel 718 nickel-based superalloy using plasma electrolytic polishing. Surf Coat Technol 441:128506. https://doi.org/10.1016/j.surfcoat.2022.128506

13. Parfenov EV, Farrakhov RG, Mukaeva VR, Gusarov AV, Nevyantseva RR, Yerokhin A (2016) Electric field effect on surface layer removal during electrolytic plasma polishing. Surf Coat Technol 307:1329–1340. https://doi.org/10.1016/j.surfcoat.2016.08.066

14. Zeidler H, Böttger Hiller F (2022) Plasma-electrolytic polishing as a post-processing technology for additively manufactured parts. Chem Ing Tec 94:1024–1029. https://doi.org/10.1002/cite.202200043

15. Huang Y, Wang C, Ding F, Yang Y, Zhang T, He XL, Zheng LJ, Li NT (2021) Principle, process, and application of metal plasma electrolytic polishing: a review. Int J Adv Manuf Technol 114:1893–1912. https://doi.org/10.1007/s00170-021-07012-7

16. Küenzi A, Goetschi M, Nelis T, Bessire C (2022) Jet application of plasma electrolyte polishing. Procedia CIRP 113:525–529. https://doi.org/10.1016/j.procir.2022.09.172

17. Kranhold C, Kröning O, Schulze H-P, Herzig M, Zeidler H (2020) Investigation of stable boundary conditions for the jet-electrolytic plasma polishing (Jet-ePP). Procedia CIRP 95:987–992. https://doi.org/10.1016/j.procir.2020.02.294

18. Wu Y, Wang L, Zhao J, Zhang C (2022) Spray electrolyte plasma polishing of GH3536 superalloy manufactured by selective laser melting. Int J Adv Manuf Technol 123:2669–2678. https://doi.org/10.1007/s00170-022-10283-3

19. Parfenov EV, Yerokhin A, Nevyantseva RR, Gorbatkov MV, Liang CJ, Matthews A (2015) Towards smart electrolytic plasma technologies: an overview of methodological approaches to process modelling. Surf Coat Technol 269:2–22. https://doi.org/10.1016/j.surfcoat.2015.02.019

20. Susanne Q, Oliver K, Daniel S, Henning Z, Igor D, André M, Falko B, Shai E, Andreas S (2022) Design and setup of a jet-based technology for localized small scale Plasma electrolytic Polishing. J Manuf Process 75:1123–1133. https://doi.org/10.1016/j.jmapro.2022.01.064

21. Zhan S, Lyu Z, Dong B, Liu WD, Zhao YH (2023) Cathodic discharge plasma in electrochemical jet machining: phenomena, mechanism and characteristics. Int J Mach Tools Manuf 187:104015. https://doi.org/10.1016/j.ijmachtools.2023.104015

22. Duan HD, Sun HW, Ji GQ, Yang DL, Li SX,Wang J, Xiang YX (2022) Biological corrosion resistance and osteoblast response of 316LVM polished using electrolytic plasma. Coatings 12:1672. https://doi.org/10.3390/coatings12111672

23. Yerokhin A, Mukaeva VR, Parfenov EV, Laugel N, Matthews A (2019) Charge transfer mechanisms underlying contact glow discharge electrolysis. Electrochim Acta 312:441–456. https://doi.org/10.1016/j.electacta.2019.04.152

24. Hasan N, Antao DS, Farouk B (2014) DC negative corona discharge in atmospheric pressure helium: transition from the corona to the 'normal' glow regime. Plasma Sources Sci Technol 23:035013. https://doi.org/10.1088/0963-0252/23/3/035013

25. Lebedev YuA, Tatarinov AV, Epstein IL, Averin KA (2016) The formation of gas bubbles by processing of liquid n-heptane in the microwave discharge. Plasma Chem Plasma Process 36:535–552. https://doi.org/10.1007/s11090-015-9685-y

26. Yoon S-Y, Jang YC, Lee S-H, Hong J, Hong YK, Kim GH (2012) Characteristics of vapor coverage formation on an RF-driven metal electrode to discharge a plasma in saline solution. Plasma Sources Sci Technol 21:055017. https://doi.org/10.1088/0963-0252/21/5/055017

27. Belkin PN, Kusmanov SA, Parfenov EV (2020) Mechanism and technological opportunity of plasma electrolytic polishing of metals and alloys surfaces. Appl Surf Sci Adv 1:100016. https://doi.org/10.1016/j.apsadv.2020.100016

28. Xin Y, Liu J, Wang Q, Sun B (2022) Plasma characteristics of atmospheric pinhole discharge in water. Vacuum 202:111181. https://doi.org/10.1016/j.vacuum.2022.111181

29. Hayashi Y, Takada N, Kanda H, Goto M (2015) Effect of fine bubbles on electric discharge in water. Plasma Sources Sci Technol 24:055023. https://doi.org/10.1088/0963-0252/24/5/055023

30. Danilov I, Hackert-Oschätzchen M, Zinecker M et al (2019) Process understanding of plasma electrolytic polishing through multiphysics simulation and inline metrology. Micromachines 10:214. https://doi.org/10.3390/mi10030214